Laser spectroscopy measurement of the 2s-hyperfine splitting in lithium-like bismuth

Rodolfo Sánchez[1], **Matthias Lochmann**[1,2,3], **Raphael Jöhren**[4], **Zoran Andelkovic**[1], **Denis Anielski**[4], **Benjamin Botermann**[1,3], **Michael Bussmann**[5], **Andreas Dax**[6] ∗, **Nadja Frömmgen**[3], **Christopher Geppert** [2,3], **Michael Hammen**[2], **Volker Hannen**[4], **Thomas Kühl**[1,7], **Yuri A. Litvinov**[1], **Rubén López-Coto**[4] †, **Thomas Stöhlker**[1,7], **Richard C. Thompson**[8], **Jonas Vollbrecht**[4], **Weiqiang Wen**[9], **Christian Weinheimer** [4], **Elisa Will**[3], **Danyal Winters**[1] and **Wilfried Nörtershäuser**[2,3]

[1] GSI Helmholtzzentrum für Schwerionenforschung GmbH, 64291 Darmstadt, Germany.

[2] Institut für Kernphysik, Technische Universität Darmstadt, 64289 Darmstadt, Germany.

[3] Institut für Kernchemie, Johannes Gutenberg-Universität Mainz, 55128 Mainz, Germany.

[4] Institut für Kernphysik, Westfälische Wilhelms-Universität Münster, 48149 Münster, Germany.

[5] Helmholtz-Zentrum Dresden-Rossendorf, 01314 Dresden, Germany.

[6] Department of Physics, University of Tokyo, Japan.

[7] Helmholtz-Institut Jena, 07743 Jena, Germany.

[8] Department of Physics, Imperial College London, London SW7 2AZ, United Kingdom.

[9] Institute of Modern Physics, Lanzhou 730000, China.

E-mail: `r.sanchez@gsi.de`

Abstract. We have recently reported on the first direct measurement of the $2s$ hyperfine transition in lithium-like bismuth $^{209}\text{Bi}^{80+}$. Combined with a new measurement of the $1s$ hyperfine splitting in the hydrogen-like $^{209}\text{Bi}^{82+}$ the so-called specific difference $\Delta'E = -61.37(36)$ meV was determined and is in good agreement with the strong-field bound-state QED prediction. Here we report on additional investigations performed to estimate systematic uncertainties of these results and on details of the experimental setup. We show that the dominating uncertainty arises from the insufficient knowledge of the ion beam velocity determined from the electron-cooler voltage. Two routes to obtain a cooler-voltage calibration are discussed and it is shown that agreement in $\Delta'E$ with the QED calculations and of the hyperfine splitting in hydrogen-like bismuth as reported in the first measurement in 1994 are mutually exclusive.

∗Present address Paul Scherrer Institut, 5232 Villingen, Switzerland.

†Present address Max-Planck-Institut für Kernphysik, 69029 Heidelberg, Germany

PACS numbers: 32.10.Fn, 31.30.J-

1. Introduction

The fundamental theory of the interaction between light and matter, also known as quantum electrodynamics (QED), is about to celebrate its 70 years of success in modern physics. Throughout these seven decades QED has conquered all tests and therefore it is considered as the most precisely tested theory in physics. Impressive examples of these tests include the high accuracy measurements of the electron g-factor [2], the Lamb-Shift in hydrogen [3][4], the 2S hyperfine interval in atomic hydrogen [5], the recent g_J-factor measurements in hydrogen-like Si^{13+} [7] and the "isotope shift" of the electron bound state g-factor in $^{40,48}Ca$ [8]. Measurements with moderate accuracy are presently also available in highly charged heavy systems, like for example x-ray spectroscopy on hydrogen-like U^{91+} [9] and lithium-like U^{89+} [10]. With the exception of the proton radius puzzle [11, 12] and deuteron radius puzzle [6], where the origin of the discrepancy with other experiments is still unclear, one can clearly state that QED is so far in accordance with all experimental results. However QED-tests in the regime of extreme magnetic fields, which are as large as 10^{10} T on the surface of heavy atomic nuclei and on neutron stars, were missing up to now. These are complementary to all other tests and can be accessed via measurements of the hyperfine splitting (HFS) and the g_J-factors from s-electrons in highly charged heavy ions. The hyperfine splitting operator shows a characteristic radial dependence of $1/\langle r^{-2}\rangle$, leading to average magnetic fields of $10\,000$ T for an electron in the $1s$ orbital, whereas the g_J-factor has a radial dependence of $\langle r\rangle$. Therefore the hyperfine splitting is considerably more sensitive to the strong magnetic fields close to the nucleus [13]. While the splitting in hydrogen is $1420.405\,751\,766\,7(9)$ MHz (see e. g. [21]) between the $F = 0, 1$ hyperfine levels, the corresponding splitting in hydrogen-like ions increases with Z^3. At the same time, the lifetime of the upper hfs state decreases with Z^{-9} from 11 Ma for the $F = 1$ state in hydrogen to $397\,\mu$s for the $F = 5$ state in hydrogen-like bismuth. Therefore some nuclei with $Z \geq 70$ exhibit a hyperfine transition in the optical regime and the lifetime becomes sufficiently short to perform laser spectroscopy even though at extremely low scattering rates. Hydrogen-like $^{209}Bi^{82+}$ exhibits the largest ground-state hyperfine splitting of all stable isotopes. It was experimentally determined to be $\Delta E^{(1s)} = 5084.1(8)$ meV, corresponding to a transition wavelength of $\lambda^{(1s)} = 243.87(4)$ nm by collinear laser spectroscopy at the experimental storage ring (ESR) [14]. This value has to be compared with the theoretical prediction for which the individual contributions are listed in table 1. The strong relativistic effects and the correction for the finite nuclear charge distribution can be handled with high accuracy, but the influence of the magnetic moment distribution (Bohr-Weisskopf effect) is much less under control. It is only on the 1% level but its relative uncertainty is almost 50% and therefore it dominates the total uncertainty and is of similar size as the complete one-electron QED contribution. Even though the measurement accuracy [14] is about 30 times more accurate than theory, its accuracy cannot be exploitet to test QED.
    Measurements of the $1s$ hyperfine splitting in other hydrogen-like heavy ions were

Table 1. Contributions to the hyperfine splitting $\Delta E^{(1s)}$ in hydrogen-like bismuth as predicted by theory. Values taken from [22]

Contribution	Size [meV]
Fermi value (non relativistic)	2747.9(1)
Relativistic value	5839.3(3)
Corrections	
Nuclear charge distribution	−648.2(7)
Bohr-Weisskopf effect	−61(27)
One-electron QED	−30.1
Total (theory)	5100(27)
Experiment	5084.1(8) [14]

carried out with similar accuracy . Hydrogen-like lead was also measured by laser spectroscopy at the ESR [15] while holmium, rhenium and thallium were determined by passive emission spectroscopy in an electron beam ion trap (EBIT) at LLNL [16, 17, 18]. Since all corresponding theoretical calculations are similarly affected by the Bohr-Weisskopf effect a high precision test of QED calculations in the strong magnetic field regime are still pending

While the Bohr-Weisskopf contribution cannot be accurately calculated, the ratio of the corrections in the $2s$ hyperfine splitting in a lithium-like ion and the $1s$ splitting in a hydrogen-like ion can be precisely calculated since it is dominantly a function of the atomic structure [25]. It was therefore proposed to employ a so-called "specific difference" between the hyperfine splittings in the hydrogen-like ion, $\Delta E^{(1s)}$, and in the lithium-like ion, $\Delta E^{(2s)}$, defined as [19]

$$\Delta' E = \Delta E^{(2s)} - \xi \Delta E^{(1s)}. \tag{1}$$

The isotope-dependent parameter $\xi = 0.16886$ (for ^{209}Bi) is chosen to completely eliminate the Bohr-Weisskopf contribution and can be calculated with high accuracy (therefore it has no uncertainty). Table 2 summarizes the different contributions to $\Delta' E$ for ^{209}Bi. It is dominated by the difference in the Dirac values and the interelectronic interaction (expanded in $1/Z$), which appears only in the Li-like charge state. Both contribute about 50% to the total value. The one-electron QED is unfortunately largely canceled in $\Delta' E$ and its contribution is on the $5 \cdot 10^{-4}$ level, roughly five times smaller than the QED contributions arising from electron-electron interactions (screened QED). The advantage of this approach is twofold:

- Measuring the hyperfine splittings in both charge states at an accuracy of about 10^{-6} will allow a sensitive test of screened QED and single-electron QED, which is not affected by finite-size effects.
- Using $\Delta E^{(1s)}$ from [14] and $\Delta' E$ one can predict an accurate value of $\Delta E^{(2s)} = 797.16(14)$ meV for the hyperfine splitting in Li-like bismuth with an uncertainty completely dominated by the experimental uncertainty of $\Delta E^{(1s)}$. The splitting

Table 2. Individual contributions to $\Delta'E$ in meV for ^{209}Bi. Values are taken from [26]. The first uncertainty originates from the calculations while the second one comes from nuclear effects, which do not completely cancel in the specific difference.

Effect	$\Delta E^{(2s)}$	$\xi \Delta E^{(1s)}$	$\Delta'E$
Dirac value	844.829	876.638	-31.809
QED	-5.052	-5.088	0.036
Interel. interaction $\sim 1/Z$	-29.995		-29.995
Interel. interaction $\sim 1/Z^2$	0.258		0.258
Interel. interaction $\sim 1/Z^3$	$-0.003(3)$		$-0.003(3)$
Screened QED	0.193(2)		0.193(2)
Total			$-61.320(4)(5)$

corresponds to a transition wavelength of $\lambda^{(2s)} = 1555.32(27)\,$nm, an information that strongly facilitated the search for the transition at the ESR.

The only experimental value reported previously for $\Delta E^{(2s)} = 820(26)$ meV was indirectly obtained in a SuperEBIT [20], deduced from the hyperfine splitting in the $2s_{1/2} - 2p_{1/2}$ x-ray transition. The uncertainty is much too large to allow for any test of $\Delta'E$ and therefore a program was initiated at GSI to measure this hyperfine transition with higher accuracy. Despite the very precise prediction of the splitting, three attempts to observe the $2s$ hyperfine transition in lithium-like bismuth by laser spectroscopy at the ESR failed between 1998 and 2004. This triggered many speculations including even doubts in the calculations of the hyperfine splitting as well as doubts of QED calculations in the presence of strong magnetic fields. The experiment is challenging since the transition rate between the $2s$ levels is only

$$w = 1/\tau = 12.2(2) \text{ s}^{-1}, \tag{2}$$

and therefore two orders of magnitude smaller than the one in hydrogen-like bismuth [25]. Moreover, the transition wavelength is in the infrared region and the photon detection is considerably less efficient and is disturbed by higher noise levels. This endeavour took 3 years of apparatus development, 10 days of beam time and 3 years for studying potential systematical errors. Only a brief description and the final results were provided in the previous publication [1]. Here we discuss all systematic uncertainties that have been evaluated. Therefore, a more detailed description of the experimental setup than that provided in [1] is necessary. The determination of statistical and systematic uncertainties is generally one of the most important tasks in an experiment that searches for deviations from theoretical predictions. We have made numerous checks to investigate possible changes of the observed transition wavelengths under varying experimental parameters. It turned out that the dominating uncertainty arises from the limited knowledge of the ion velocity. Its influence onto the specific difference determined in the experiment and the conclusions that can be drawn from the results are discussed in greater detail.
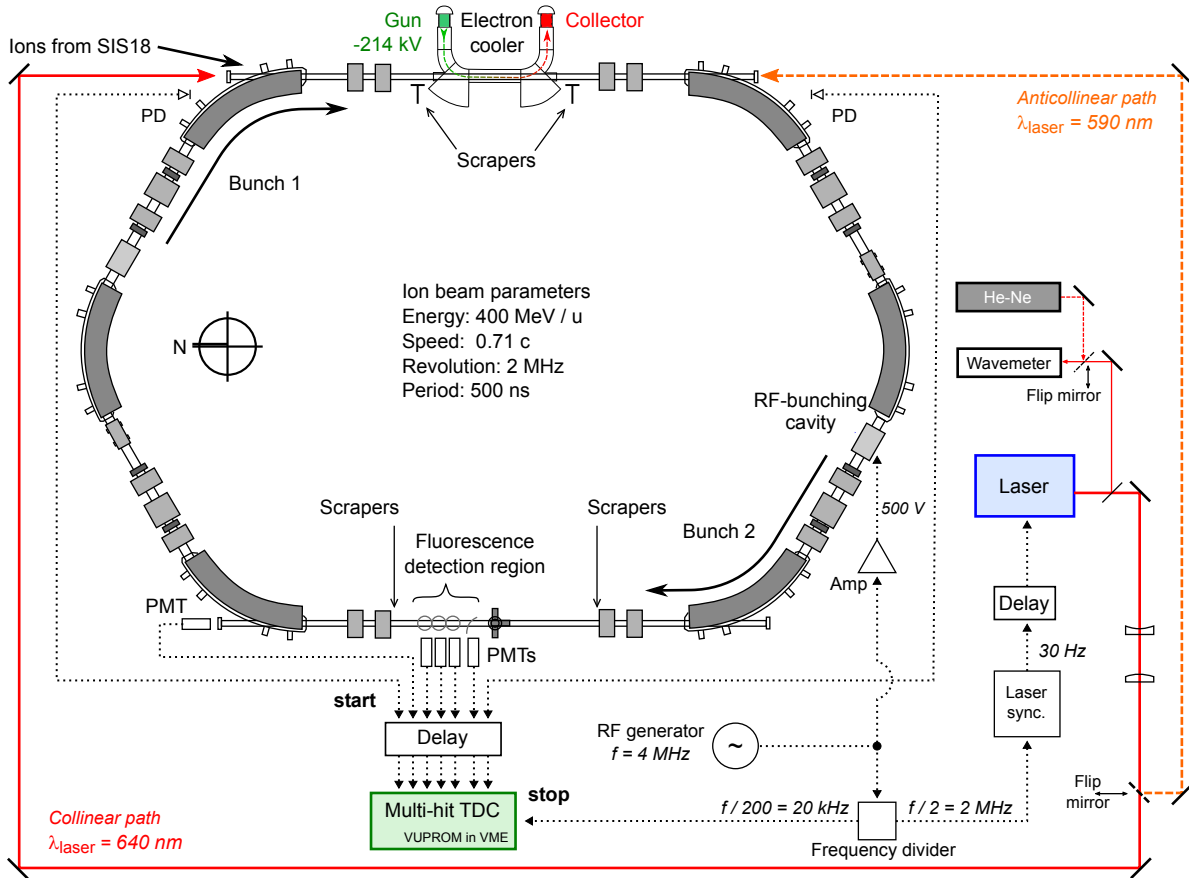
Figure 1. Schematic view of the ESR and the experimental setup including the laser and data acquisition system. Laser beam paths are shown as solid and dashed lines while electrical signals are represented by dotted lines. A detailed description of the setup is given in the text.

2. Experimental Setup

Figure 1 shows a schematic view of the experimental storage ring at GSI [31], with the main components for laser spectroscopy of the $F = 4 \to F = 5$ M1 hyperfine transition in the 1s and 2s ground states in hydrogen-like and lithium-like bismuth, respectively. In the following sections the individual parts of the experimental setup are described in more detail.

2.1. Production of the H- and Li-like bismuth

Multiply charged (Bi^{4+}) ions were produced using a metal vapor vacuum arc (MEVVA) ion source [32] and afterwards accelerated by the linear accelerator UNILAC∗ before they were transferred to the synchrotron SIS-18†, where they were further accelerated to an energy of about 400 MeV/u. After extraction they passed a thin stripping foil,

∗UNILAC: Universal linear accelerator.
†SIS: Schwerionensynchrotron (heavy-ion-synchrotron) with a magnetic rigidity of 18 Tm.

a copper foil with an area density of 40 mg/cm^2 or a 29 mg/cm^2 carbon foil for the production of Bi^{82+} and Bi^{80+}, respectively, and were then injected into the ESR.

2.2. Experimental Storage Ring - ESR

The ESR is shown in figure 1: The ion orbit is closed by six 60° dipole magnets while the quadrupoles are used for focusing and sextupole magnets are used to perform higher order ion optical corrections [31]. The ring is designed to have an ion-beam orbit of about 108.36 m, but the real value can vary up to 100 mm according, for example, to the ion-optic settings, the ion-charge state and the ion-beam energy. In our case the corresponding ion-revolution frequency was of the order of 2 MHz and it was measured with a 10^{-6} accuracy using a broadband Schottky spectrometer [33]. Typical ion beam currents in the ring were between 2 and 3 mA, corresponding to about 10^8 stored ions. In the electron cooler the stored ions are superimposed with an electron beam of about 50 mm diameter. To match the ion velocity the electron cooler was operated at -214 kV, close to the maximum value where it can be operated under stable conditions for extended periods of time. The length of the electron-ion interaction region is about 2 m. In this way the ions are cooled down over several seconds with "cold" electrons. The hot electron beam is collected again on the HV-platform after the interaction. Electron-cooling reduces the longitudinal momentum spread of the ions [34] and therefore the resonance linewidth in the laboratory frame. This leads to a more efficient excitation and a reduction of the ion beam diameter.

As shown in figure 1, the ring has two straight sections which extend outside the dipole magnets. These vacuum tubes end in axial windows for optical access. Laser beams can be coupled either in a co-propagating (collinear) or counter-propagating (anticollinear) configuration with respect to the ion beam direction. For this experiment, the laser-ion interaction region was located at the electron-cooler side of the ring. Utilizing the Doppler shift $\lambda_{\mathrm{L}} = \lambda_0 \gamma (1 - \beta \cos \theta)$ in the collinear ($\theta = 0°$) and anticollinear ($\theta = 180°$) configuration the transition frequencies are shifted in the laboratory frame from 1555 nm to 640 nm (lithium-like, collinear) and from 243 nm to 590 nm (hydrogen-like, anticollinear). Hence, both hyperfine transitions can be addressed with one laser system, as described in section 2.3. In order to increase the excitation efficiency and to reduce the background level, the ions were collected in two bunches revolving in the ESR with a phase shift of 180°. To this aim the second harmonic of the revolution frequency is applied to one of the two RF cavities in the ring. The length of the ion bunch is approximately 10–12 m [36, 37]. One bunch is repeatedly irradiated at a repetition rate of 30 Hz by the laser along the electron cooler section, while the second bunch (reference bunch) is located at the opposite side of the ring at the optical detection region. Photons observed when the reference bunch is passing the detection region originated from collisional excitation of residual gas atoms. It can be utilized to detect the arrival of a bunch at this region as discussed below. Half a revolution period later ($\sim$ 250 ns) the excited bunch passes the optical detection region

while the reference bunch is at the electron cooler. Even for hydrogen-like bismuth with a half-life on the order of 560 μs in the laboratory frame [38] the fluorescence lasts for more than 1000 revolutions and the fluorescence photons have to be collected all the time with respect to the signal bunch position as discussed below.

2.3. Laser setup

M1 transitions with lifetime in the ms regime have a linewidth of only 100 Hz. This combined with the large Doppler broadening requires a laser with a large bandwidth and high pulse-power in order to efficiently excite a large fraction of the revolving ions. The light for both transitions was produced by a pulsed dye laser∗ pumped with up to 600 mJ of the second harmonic of a Nd:YAG laser†. The dye laser was customized for this experiment: It was used in the Litrow configuration with a grating of 1800 lines/mm, which could be illuminated either partially or completely in order to obtain laser bandwidths of about 2.0 cm^{-1} ($\approx$ 60 GHz) used during the search for the first resonance signal or of 0.64 cm^{-1} for spectroscopy. Sulforhodamin B dissolved in ethanol at a concentration of 0.2 g/l was used in the oscillator and preamplifier cell when operated for hydrogen-like bismuth while 0.3 g/l DCM dissolved in a solution of 50% Ethanol and 50% DMSO was used for lithium-like bismuth. The dye concentration in the main amplifier was in both cases 1/8 of that in the oscillator in order not to damage the glass of the dye cell. Typical pulse energies of 120 mJ and 150 mJ were obtained at the operation wavelength of 590 nm and 641 nm, respectively. The wavelength of the laser was monitored continuously using a wavemeter of the Fizeau interferometer type‡, which was calibrated regularly during the beamtime with a stabilized and calibrated He:Ne laser.

For transport along the 50 m and 80 m distances to the interaction region of the ESR, the laser beam was expanded using a telescope consisting of a plano-concave lens with a focal length of $f = -400$ mm and a plano-convex lens with $f = +800$ mm in a distance of about 400 mm that was fine tuned to obtain a spot of about 15 mm FWHM at the electron cooler position. In order to change from the anticollinear to the collinear configuration a flip mirror was used as it is schematically shown in figure 1. Laser transport was realized using 3" mirrors and the overlap between the ion beam and the laser beam was realized after optimization of the ESR ion-optical parameters and the electron cooling. Therefore, the ion beam position was determined with two scrapers (T-shape) which are located inside the electron cooler in a distance of $\approx$ 4 m and symmetrically with respect to the electron-cooler center position. The alignment of the laser beam was then fine-tuned with reference to these scraper positions. While the ion beam center can be determined with an accuracy better than 1 mm, this is slightly worse for the laser beam due to its size and the diffraction pattern that occurs when

∗Sirah, Cobra Stretch G-1800
† Spectra Physics, Quanta Ray Pro 290-30
‡ATOS, LM007

the scrapers are moved into the beam. The precision of the determination of the beam center is estimated to be better than $\pm 2\,\text{mm}$, corresponding to a maximum angular deviation of about $1\,\text{mrad}$ between the laser and the ion beam. However, it must be taken into account that the laser overlaps the ion beam along the complete straight section and excitation can occur everywhere along this section. Due to the quadrupole and the toroids at the electron cooler, the ion beam slightly changes the direction along the beam path which can leads to small angular deviations. It is estimated from ion optical simulations that between the two quadrupoles a deviation of up to $2.7\,\text{mrad}$ can occur. This is also the maximum angle that can be realized with the laser with respect to the central orbit if the 60-mm free apertures of the two windows and the distance of $23\,\text{m}$ between those is considered. The position and pointing stability of the laser at the interaction region was ensured by active stabilization with a commercial system∗. For this purpose, a small fraction of the laser beam was splitted off the main beam in front of the entrance viewport of the ESR and further divided into two beams by using wedge plates. One of these beams was fed in the stabilization system while the second spot was sent to a screen in a distance equivalent to the distance to the center of the electron cooler. The focus position and form was visually observed from the control center as well as the size and position of the main beam after exiting the window at the other side of the straight section. Hence we were able to limit beam excursions at the electron cooler to less than $\approx \pm 3\,\text{mm}$ and changes of the angle to less than $1\,\text{mrad}$.

2.4. Fluorescence Detection

Due to the long lifetime of the transitions (Bi^{82+}: $\tau \approx 0.4$ ms [39], Bi^{80+}: $\tau \approx 82$ms [25]) compared to the ion revolution time in the storage ring of about $t_{\text{Rev}} \approx 250$ ns, fluorescence detection is performed on the opposite side of the ESR to be completely free from scattered laser light.

At relativistic velocities the isotropic emission in the ion rest frame is transformed into an emission cone in the forward direction due to the relativistic aberration. The observed flux ϕ in the laboratory frame under angle θ with respect to the ion velocity is changed by a factor D^3

$$\frac{\phi_0(\theta_0)}{\phi(\theta)} = D^3 = \left(\frac{\lambda}{\lambda_0}\right)^3, \tag{3}$$

where the index 0 denotes the rest frame of the ion and D is given by

$$D = \frac{1}{\gamma(1 - \beta \cos\theta)}. \tag{4}$$

At a velocity of $\beta = 0.71$ this increases the flux in the forward direction by a factor of 5.9, and reduces it to 50% and 17% in perpendicular and backward directions, respectively. Additionally, the photon wavelength changes as a function of the emission

∗TEM, Aligna

angle in the laboratory frame according to $\lambda = D\lambda_0$. In figure 2(d) a two-dimensional projection of the fluorescence distribution in the laboratory frame is shown for the case of Bi^{80+}. The length of the arrow indicates the intensity boost and the color code indicates the wavelength. For hydrogen-like ions this leads to a λ-variation from 591 nm (laser wavelength) to 100 nm from backward to forward angles. The transmission curve of the quartz window and the spectral sensitivity of the UV-sensitive ("solar blind") photomultiplier tube (PMT)∗ sensitive in the wavelength regime 120 nm $\leq \lambda \leq$ 350 nm that was used for Bi^{82+} restricts detection sensitivity to those photons emitted between about 54° ($\lambda >$ 200 nm) and 79° ($\lambda <$ 370 nm) in the forward direction. A schematic drawing of the mirror system used for Bi^{82+} is shown in figure 2(a). It consists of 10 segmented aluminum sheets. The foils are geometrically arranged to enhance the reflection of the fluorescence photons emitted between 20° and 60° with respect to the ion beam direction towards the optical viewports (W2-W4), which are equipped with PMTs. One "solar blind" PMT was installed at port W2 (see figure 2(a)).

Detection of the fluorescence emitted by the lithium-like bismuth ions in the ring is considerably more challenging. The corresponding fluorescence rate is more than two orders of magnitude smaller and the infrared transition wavelength of $\lambda \approx$ 1555 nm in the rest frame is shifted to 3.77 μm in backward and 641 nm (laser wavelength) in forward direction. To detect these photons, red-sensitive PMTs† were used and cooled down to about -20 °C to further suppress background light. The sensitivity of this PMT restricts photon detection to wavelengths of 641 $\leq \lambda \leq$ 790 nm and corresponding emission angles between $0 \leq \theta \leq$ 25°. Simulations of the segmented mirror system indicated that the fluorescence collection efficiency, under these angles is insufficient [40].

Hence a new detection system was developed that is shown in figure 2(b) and 2(c) and is described in detail in [40]. It consists of an off-axis parabolic mirror mounted on a retractable linear feedthrough. The mirror has a diameter of 150 mm and is made of copper since this material has a reflectivity of

$R = (89 \pm 4)\%$ in the range 600–700 nm and is compatible with UHV conditions inside the storage ring. The mirror has a central cut to allow the ions to pass through but the fluorescence emitted at small angles to the forward direction is collected and directed towards the PMT. Therefore the detection probability for photons emitted at angles $\leq$ 25° with respect to the ion-beam direction that fall within the quantum efficiency of the PMT is dramatically increased. An additional reflecting cone, as depicted in figure 2(b), is installed to further enhance the collection efficiency. The reflected fluorescence passes through a window and a light-guide, before it reaches the red-sensitive PMT mounted at the viewport W1. The full aperture of the central cut is 30 mm and was chosen to be 3× the FWHM the typical radius of an electron-cooled

---

∗Thorn EMI, 9422A

†Hamamatsu R1017, equipped with a combination of a NIR-blocking Calflex X (LINOS) and a long-pass filter RG590 (Schott) joined with each other and with the PMT viewport using optical grease.
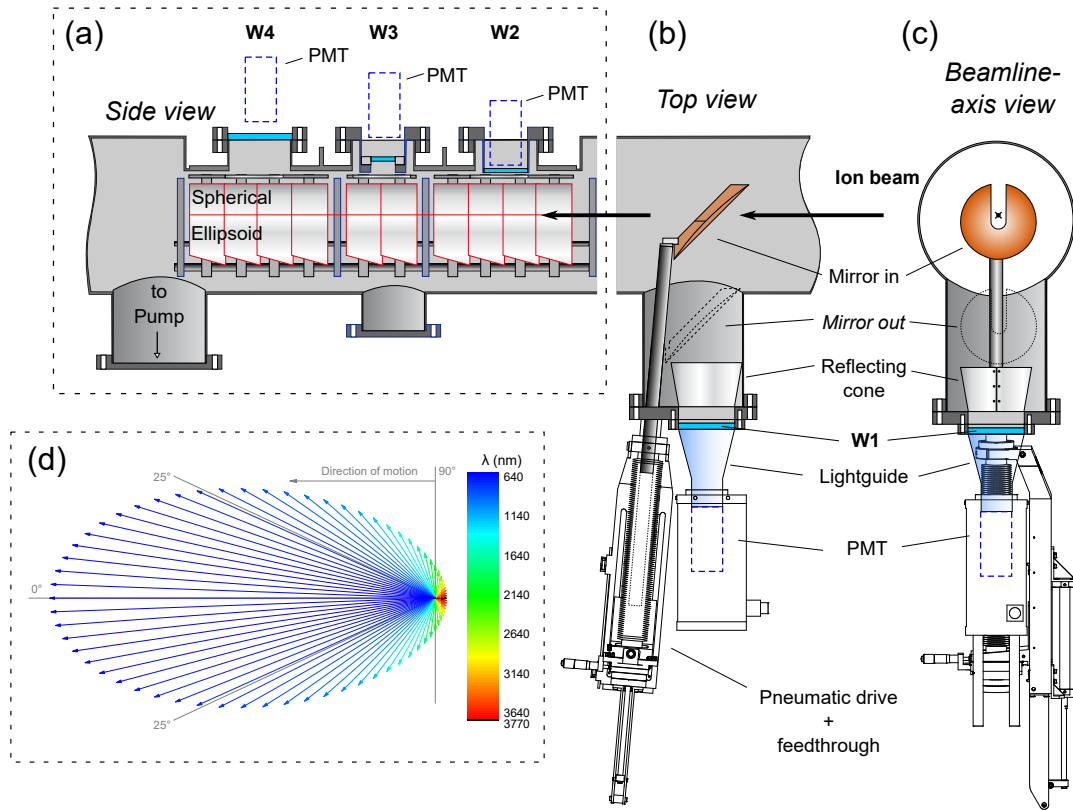
Figure 2. Schematic view of the two mirror systems for fluorescence detection at the ESR. Its location at the ring is opposite to the electron-cooler side (see figure 1). (a) Side view of the detection system for H-Like Bi: the inner part of the beam tube is lined with UV reflective material in a cylindrical (upper part) and ellipsoidal (lower half) form. The lower part is tilted by 15° towards the ion direction in order to reflect the mainly forward emitted light towards the three windows (W2-W4) on top of the beam tube where PMTs can be mounted. During the beamtime, for H-like Bi, window W2 was equipped with a UV-sensitive PMT (solar blind). Afterwards on W2 to W4 red-sensitive PMTs were mounted to search for the fluorescence of the Li-like ion also with this detection system. (b) Top view of the detection system for Li-like Bi which is mounted in front of that for H-like Bi: the copper mirror is mounted horizontally at the vacuum port and the photons are deflected sideways towards the window (W1) where a lightguide connected to the red-sensitive PMT is mounted. The mirror is shown in the detection position *Mirror out*. During injection and cooling the mirror is moved into the position marked as *Mirror out*. (c) front view of (b) along the beamline axis, the position where the ions pass through the slit in the mirror is marked with a cross. (d) Relativistic aberration and Doppler shift of the fluorescence detected in the laboratory frame assuming isotropic emission of the HFS transition of Li-like Bi in the ions rest frame. The color scale represents the Doppler shifted wavelength in the laboratory frame and the length of each arrow is proportional to the relative number of photons emitted under the respective solid angle.

ion-beam of about 10 mm FWHM. Since the ion beam might have considerably larger diameter after injection from SIS, the mirror is moved out of the beam for ion injection and initial cooling. Once the beam is cooled, the mirror is moved in place in about 1 s. Typically a loss of less than 10% of the ion beam is observed during this process.

It should be noted that for the search of the fluorescence of Bi^{80+}, red-sensitive PMTs were mounted on all three windows (W2-W4) of the segmented-mirror section as well. However, no fluorescence signal was observed at this detection region, which explains the previously failing attempts and confirms the simulations that were carried out previously [40]. Here, only the new parabolic mirror turned out to be the suitable device for signal detection of lithium-like bismuth, confirming the simulations that were carried out previously [40].

Fast moving ions induce an isotropic fluorescence background by collisions with the residual-gas molecules inside the vacuum beamline [41]. This induced-background fluorescence covers the visible region and exhibits fast ultraviolet and blue as well as slower red and infrared components and produces signals on the PMT, and can be used for timing, synchronization of the laser pulse with the ion bunch position, and the determination of the bunch length as described in [36, 37] (see below, section 2.5). However its noise level can bury the fluorescence signal.

2.5. Data Acquisition and Timing

The central development in the new data acquisition system was the time-tagging for every detected photon. It considerably simplified the synchronization and timing of all time-critical parameters and allowed for a post-beamtime optimization of the acceptance windows for fluorescence photons from the ion bunches. The ion bunches revolving inside the storage ring with a phase shift of 180° were created with a sinusoidal signal at twice the revolution frequency (~ 4 MHz) that was produced by a radio frequency (RF) generator amplified to typically 500–700 V and applied to one of the RF cavities as shown in figure 1.

A part of the RF signal for ion bunching was discriminated, divided by a factor 200 to about 20 kHz and used as a common-stop signal for a multihit multichannel time-to-digital converter (TDC) realized on a field programmable gate array (FPGA). Hence each photon has a timing information between 0 and 50 μs with a fixed phase relation to the bunching frequency. The only information required in the analysis is the arrival time of the photon within a single revolution. The FPGA has a time resolution of 10/3 ns given by its internal 300 MHz clock.

The signals of 12 detectors were recorded by the TDC. Six of these detectors were dedicated to detect the fluorescence signal. They were located at the segmented-mirror section (one UV- and three red-sensitive PMTs for spectroscopy for spectroscopy of hydrogen-like and lithium-like ions, respectively), at the parabolic mirror system (one red-sensitive PMT) and one detector in forward direction∗ at the laser beamport

∗Hamamatsu, R943-02

on the target side as shown in the lower left side of figure 1. There we looked for a fluorescence signal from photons emitted under small angles in the forward direction. The signals of these PMTs were amplified by a 16 channel fast amplifier∗ , transfered to the DAQ-room and there fed to an inductive decoupling unit† before being processed by a 16 channel constant fraction discriminator‡.

The black histogram in figure 3 shows the number of recorded PMT-pulses as a function of time till common stop modulo the revolution time. A full revolution requires about 510 ns, which are divided in 153 bins, each corresponding to a 300 MHz TDC-timing unit equivalent to 10/3 ns. Due to the prompt UV response of the collision-induced background, the solar-blind PMT was used to establish the right timing of all components, especially the laser pulse (see below). The bunch structure of the beam is clearly visible by the two prominent peaks: their maxima appear at about 125 ns and 375 ns . The peak width (FWHM) corresponds to a spatial ion-bunch length of about 7 m in the laboratory frame.

Four additional detectors were mounted at various places in the ESR: One PMT was located at the gas-jet target, two UV PMTs and a channeltron were located between the gas-jet target and the mirror section [37] (not shown in figure 1. The signals of these detectors were fed into the data acquisition in the same way as described above. In order to determine the arrival time of the laser pulse at the ESR window, two fast pin-photodiodes (PD) were mounted at this position as depicted in figure 1. The signal travel times of all PMTs and the PD detectors were matched with delay units for accurate timing, i.e., identical travel times from all detectors to the TDC.

The PD signals are discriminated and fed into the multihit TDC. A histogram of these signals is also included in figure 3. The time gap between both PD-signals is fix and represents the laser-pulse travel time through the straight section of the ESR. By changing the delay time of the trigger pulse applied to the pump laser's Pockels-cell, the positions of these signals were adjusted until they appeared symmetrically with respect to the maximum of one of the bunches. This bunch is the reference bunch, since it is located at the optical detection region while the laser pulse intersects the cooler region. (Please note that the PD's are located on the opposite side of the ring.) Due to the symmetry of the ESR it was ensured that the laser pulse coincides with the signal bunch in the electron-cooler section.

Besides the various photon detectors the only other parameter recorded by the TDC was the Q-switch signal of the pump laser.
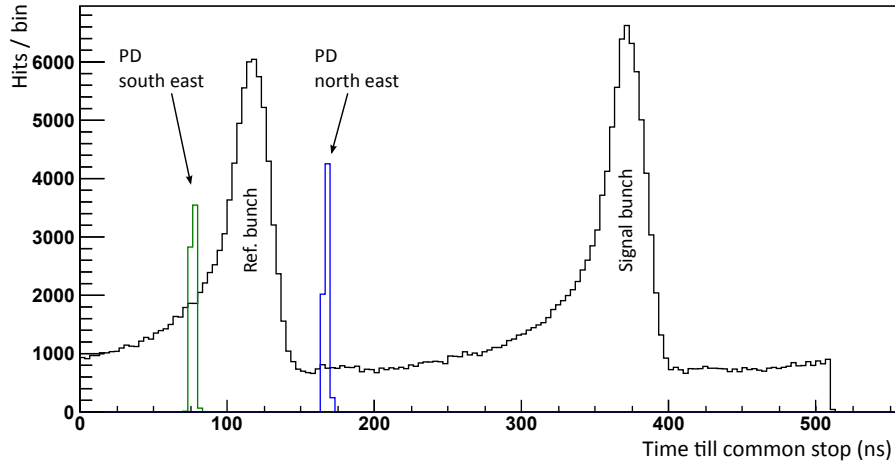
Figure 3. Profile of the bunch structure. The time delay applied to the pulsed laser is adjusted until the peaks of the photodiodes (PD) are located symmetrically around one of the ion bunch signals. Then one can be sure that the laser pulse hits only one of the bunches at the electron cooler section. Please note that the time on the x axis is inverted since the remaining time after the event until the common stop signal appeared is used. For more details see text.

3. Data analysis

The data obtained was analyzed independently using two different approaches [43, 44]. Both resulted in consistent results for the central laser wavelengths. In the following the fitting procedures are described in detail. A single scan with a scan range of $0.5\,\text{nm}$ divided into 51 steps ($\Delta\lambda = 0.01\,\text{nm}$) was typically recorded in about 5 minutes. The signal strength and the laser wavelength for each step was extracted from the raw data using the following procedure: The data of a single TDC common stop period – corresponding to 100 ion revolutions – is binned with respect to the revolution phase to obtain the bunch structure as it is shown in figure 4. Count rate uncertainties are attributed according to Poisson statistics. In [44] these histograms are fitted by two Gaussians and a constant offset. The fit function

$$f(x) = y_0 + \frac{A_1}{\sqrt{2\pi}w_1}\exp\left[\frac{(x-t_1)^2}{2w_1{}^2}\right] + \frac{A_1 + \Delta A}{\sqrt{2\pi}w_2}\exp\left[\frac{(x-t_2)^2}{2w_2{}^2}\right] \qquad (5)$$

directly includes the area difference ΔA of the two Gaussians, which is proportional to the observed signal rate. Thus, the area difference and the corresponding error are obtained directly from the fitted parameters without the need to perform an error propagation of correlated uncertainties. In [43] two approaches are applied: In a first variant, both Gaussians are fitted and the areas substracted from each other to obtain
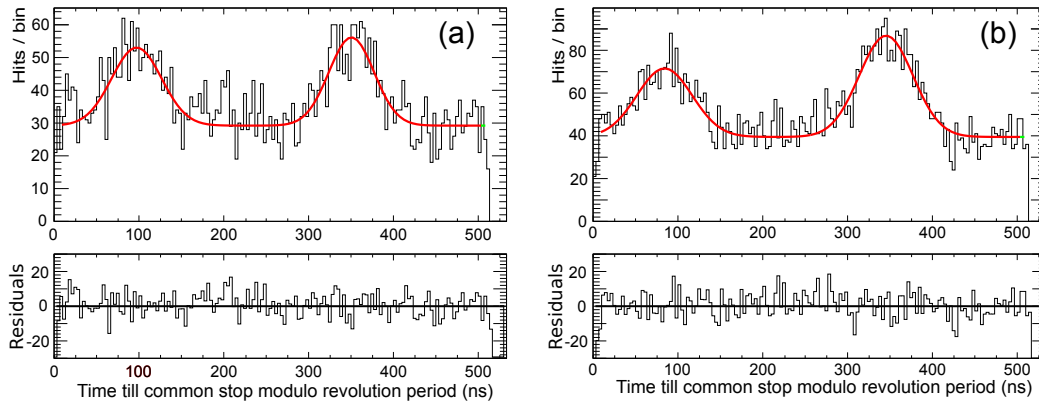
*CAEN, 979
†GSI, AP2005
‡CAEN, N843

Figure 4. Two examples of the TDC histogram fits: (a) is taken with the laser slightly off resonance and therefore the peak of the reference bunch has approximately the same area as that of the signal bunch. (b) Is taken on resonance and the area and amplitude of the signal bunch peak is clearly larger than that of the reference bunch. More details in text.

the signal rate. In a second approach, the number of counts located in a specified region of interest of the two peaks, chosen to be symmetric about the central peak position, are counted and substracted from each other without any fitting.

For each wavelength step the mean laser wavelength λ_{step} along with its uncertainty $\Delta\lambda$ as well as the mean laser intensity I_{laser} is calculated from all wavemeter data recorded during the corresponding time interval. The resonance structure is then obtained by plotting the area differences of the TDC data normalized to the ion current and the measuring time, as a function of the laser wavelength. A Gaussian profile is then fitted to the resonance curve Since several scans are combined to a single spectrum, but the wavelength information of the individual scans is not identical, the combination is performed using two strategies in [44]: (1) To avoid binning problems, every data point is plotted with its individual wavelength. (2) Alternatively, a binned version of the data is produced: Therefore the normalized count rate of each step multiplied with the actual ion current is splitted into two fractions depending on the relative position of the step's wavelength between two neighboring bins of the histogram. By dividing the measuring time in the same fashion, multiplied also with the actual ion current, the signal rates are again normalized to cps/mA. Figure 5 shows an example of the corresponding datasets and the fits; the central value of the Gaussian along with its uncertainty denotes the fitted transition wavelength λ_{fit} with the error $\Delta\lambda_{\text{fit}}$. The residuals are normalized to the uncertainty of the corresponding data point σ_i. The results of both strategies agree within their uncertainties. Three strategies are used in [43]: (1) each individual scan was fitted independently, even when the signal was weak, (2) combining three scans with the classical histogramming approach without data distribution as described above and (3) simultaneous fitting of three scans with individual wavelength information for each data point. The results of all approaches do not show any systematic differences. [44]

Generally, the fits yielded full-widths at half-maximum of $\approx 100\,\mathrm{GHz}$ and statistically distributed fit residuals.
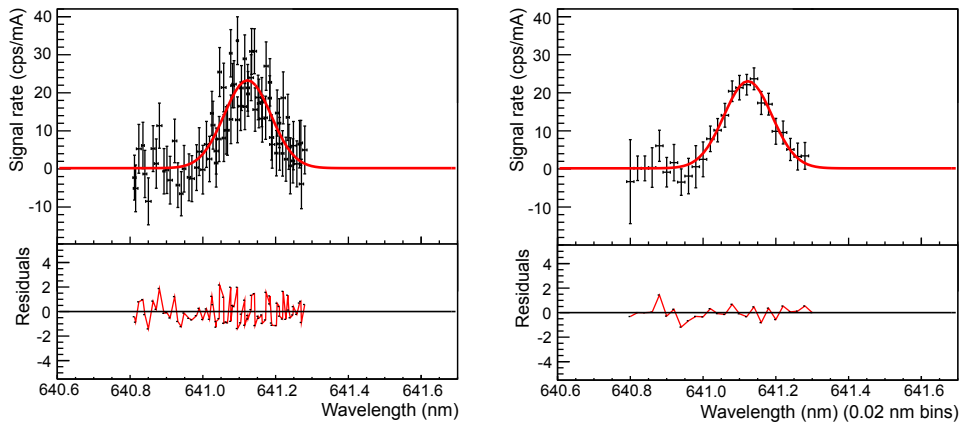

Figure 5. Examples of the resonance fit of a single spectrum. The left plot shows the fit of the unbinned data, while the right one is binned with a bin width of $0.01\,\mathrm{nm}$.

4. Results

During the beamtime, resonances were recorded under various experimental conditions in order to investigate possible systematic shifts of the central resonance wavelength. Especially the influence of the ion beam current, the electron cooler current, and the RF amplitude for bunching have been addressed. All resonances of lithium-like and hydrogen-like bismuth have been analyzed using the procedure described in the previous section. While the uncertainties of the center wavelengths resulting from these fits take into account only the statistical uncertainty of the data , systematic uncertainties have to be evaluated additionally. Therefore we searched for a possible dependence of the obtained resonance wavelength from the varied experimental parameter.

4.1. Transition wavelength in the laboratory frame

The determination of the resonance wavelength in the laboratory is directly affected by the wavemeter calibration and a possible tilt between ion and laser beam. Additionally, we discuss also the small variations that might appear from a change in the bunching amplitude and the ion beam current in this section and determine the arising combined systematic uncertainty. Afterwards, we treat the uncertainty in the determination of the ion velocity.

Ion beam current: Spectra were recorded for typical ion beam currents between 1.5 and 3.0 mA and some spectra were also recorded for 0.5 mA. All the values were obtained for an RF voltage amplitude of 500 V. The central wavelength was then plotted as a function of the ion beam current and the data were fitted with a linear function. No significant dependence of the central wavelength with respect to the

ion beam current was observed, however the data scatter around the mean value by about 10 pm. In order to obtain a conservative upper limit for the uncertainty introduced by this effect, the value extrapolated at zero ion beam current was calculated and its uncertainty is obtained as $\Delta\lambda_{\text{I}-\text{ion}} = 11.5$ pm in the laboratory frame.

RF Amplitude: Spectra were recorded for different RF-voltage amplitudes applied to the RF-cavity. As explained in section 2 this leads to bunched ion beams. Here all the parameters except the RF amplitude were kept constant. Spectra were then recorded for voltage amplitudes between 100 V and 700 V in 200-V steps. Similar to the investigation of the ion-beam current dependence, the fitted central wavelength was calculated and plotted as a function of the RF amplitude. The data were then fitted with a linear function. In first approximation the central wavelength shows almost no dependence on the RF voltage amplitude. In order to get a conservative value of the systematic introduced by this effect, the maximum scatter around the standard value of $U_{\text{RF}} = 500$ V was calculated. The obtained value is $\Delta\lambda_{\text{RF}} = 6$ pm.

Angular deviation: As discussed in section 2.3, an angular uncertainty of $\Delta\theta_{\text{max}} \approx 2.6$ mrad is estimated from ion optical simulations and the maximum deviation allowed from the free aperture of the entrance and exit windows. This can be transformed to a wavelength uncertainty according to $\Delta\lambda_\theta = |\gamma\lambda_0\beta(\cos\Delta\theta_{\text{max}} - 1)|$. For the case of collinear and anticollinear spectroscopy we obtain 5 pm and 0.8 pm, respectively, in the laboratory frame.

Wavelength calibration: The laser wavelength was not actively stabilized, but measured for each individual laser shot with a wavemeter. For each wavelength step, all measured values were averaged. When the laser was operated in broadband mode, only a single Fizeau interferometer could be used while for operation with the smaller bandwidth two interferometers were used. The wavemeter exhibits a relative accuracy of 10^{-7} if it is operated with all four interferometers. In order to estimate the relative accuracy when using only one or two interferometers, the wavelength of the reference helium-neon laser was measured after the beamtime using only the restricted number of interferometers and the deviation from the nominated wavelength was obtained. Additionally, the influence of the spectral asymmetry of the pulsed dye laser was estimated to introduce a systematic uncertainty of one quarter of the FWHM of the laser linewidth, which - in the narrow configuration - is given by 26 pm. The estimated total uncertainty of the wavelength calibration is therefore $\Delta\lambda_{\text{cal}} = 17$ pm.

For hydrogen-like bismuth we have in total recorded 7 scans, which were combined in two spectra and for lithium-like bismuth 72 scans were taken and combined to 24 spectra. Error weighted averages of

$$\lambda_{\text{lab}}^{(82+)} = 591.183(26) \text{ nm} \tag{6}$$

and

$$\lambda_{\text{lab}}^{(80+)} = 641.112(24) \text{ nm} \tag{7}$$

were obtained. The total uncertainty is determined by adding the ESR-related uncertainties since these could be correlated. A systematic deviation of the wavemeter calibration can be regarded as independent and this uncertainty has finally been added in quadrature to obtain the total uncertainty.
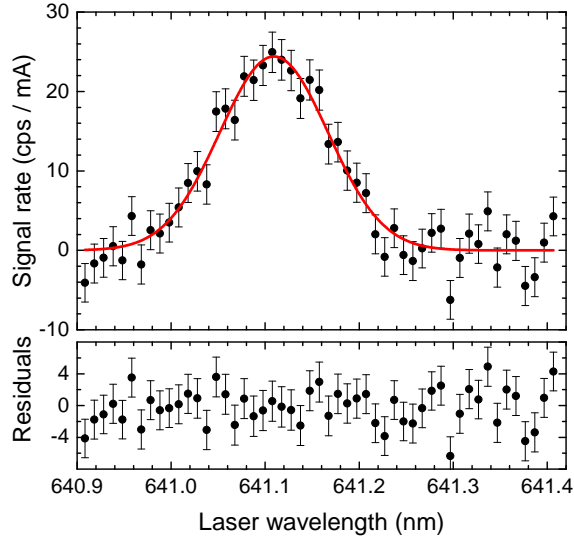

Figure 6. Resonance of the ground-state hyperfine structure transition in lithium-like Bi^{80+}. Normalized signal rate as a function of laser wavelength. The solid line is an error weighted Gaussian fit without background assumed.

4.2. Rest-frame transition wavelength

The crucial step in the analysis is the transformation from the laboratory frame into the ions' rest frame, requiring accurate information about the ion speed. In principle the ions should have adapted to the velocity of the electrons in the cooler section after sufficient cooling time [45]. The electron velocity can be determined from the electron cooler voltage using

$$\beta = \sqrt{1 - \gamma^{-2}} = \sqrt{1 - \left(1 + \frac{eU}{m_e c^2}\right)^{-2}}, \tag{8}$$

where $\beta = v/c$ is the velocity, e the elementary charge, U the electron accelerating potential difference, and m_e the electron mass. The measurements were performed at a nominal electron cooler voltage of $U_{\text{set}} = -213\,900$ V for Bi^{82+} and $-213\,890$ V for Bi^{80+}. To estimate the uncertainty of the ion velocity, the relation between the set-voltage and the applied voltage of the electron cooler high-voltage device has to be taken into account. Additional corrections for the space charge of the electron beam Φ_e according to

$$\Phi_e = \varphi \frac{I}{\beta} \tag{9}$$

and similarly for the ion beam as well as their related uncertainties must be considered.

The space charge correction of the electron beam was experimentally determined by turning off the bunching frequency, grounding the RF-cavity and varying the ion cooler current from the usually applied 200 mA down to 10 mA. This electron current is still sufficient to keep the beam cold. During this process the increasing Schottky frequency of the circulating ion beam is observed and once the 10 mA current is reached the electron cooler voltage is decreased until the original revolution frequency is covered.Here, φ is the proportionality factor for the space charge correction, I is the electron current and β the ion (and electron) velocity. The required change of voltage directly reflects the electron-beam space-charge correction and a correction factor of $\varphi_{\mathrm{exp}} = 0.111$ V/mA is obtained. This is in excellent agreement with a theoretical estimation of $\varphi_{\mathrm{theo}} = 0.112$ V/mA based on a cylindrically symmetric electron beam potential and the ion beam passing through the central potential. As discussed before, an influence of the ion beam current on the resonance wavelength was not observed and according to theoretical estimations it should be only a –4.2 V contribution which is added to the electron space charge of 31.4 V and assumed as the total space-charge correction uncertainty. The complete space charge correction therefore amounts to $\delta U_{\mathrm{space-charge}} = 27(4)$ V.

The relation between the electron-cooler set-voltage and the real voltage applied at the cooler terminal was determined with a high-voltage voltmeter (*Heinzinger*, HVDVM 131) up to -100 kV, which is its maximum operating voltage. The calibration relation had then to be extrapolated to the operation voltage of -214 kV. In order to estimate the accuracy of the voltmeter, we have analyzed the complete series of such determinations since the voltmeter was calibrated in 2001 at the *Physikalisch Technische Bundesanstalt (PTB)* in Braunschweig. This analysis pointed to a significant temporal change either of the GSI voltmeter calibration or of the electron cooler power supply during that period. Therefore, we initiated a recalibration at PTB in 2012 where also a significant shift against the 2001 calibration was observed for positive voltages. A similar drift is expected for negative voltages but could not be verified anymore due to a breakdown of the voltmeter during the calibration. We have taken into account all available information and extrapolated the high-voltage calibrations with a second-order polynomial to account for the expected quadratic dependence of the heating power $P = U \cdot I = U^2/R$ on the voltage. Based on the observed drift of the positive branch and assuming, that the asymmetry between the positive and the negative branch was conserved, we have estimated the corresponding drift on negative voltages and obtained a total calibration correction of 131 V.

Statistical and systematic uncertainties were treated independently and added in quadrature for the statistical uncertainties and linearly in the case of the systematic uncertainty, resulting in 20 V and 65 V, respectively. Finally we observed in a few test experiments as well as during a laser-cooling beamtime at the ESR [35] an occasional voltage shift of about 25 V after resetting the cooler voltage power supply. This reproducibility is taken into account as an additional uncertainty of 25 V, which is also added linearly to the systematic uncertainty. All contributions and the final value for the effective electron acceleration voltage and its uncertainty, are listed in table 3.

Table 3. Electron cooler settings used during the experiment as described in the text.

	Bi^{82+}	Bi^{80+}	Units
Electron current	200	150	mA
U_{set}	$-213\,900$	$-213\,890$	V
Calibration correction	$-132(85)$	$-132(85)$	V
Reproducibility e-cooler voltage	± 25	± 25	V
$U_{\text{e-cooler}}$	$-214\,030(110)$	$-214\,021(110)$	V
Space charge correction	$27(4)$	$19(4)$	V
Detuned bunching frequency	-	$67(5)$	V
U_{eff}	$-214\,005(110)$	$-213\,935(110)$	V
Calculated ion velocity β	$0.709\,38(29)$	$0.709\,32(31)$	

In the case of lithium-like bismuth there was an additional complication: Usually the free revolution frequency of the ions is measured in the coasting beam mode, i.e. without applying an RF voltage at the bunching cavity. Then, twice this frequency $f_{\text{RF}} = 2 \cdot f_{\text{rev}}$ is applied to the RF cavity to ensure that the RF bucket force and the electron-cooler force have the zero-crossing at the same ion speed and are therefore driving the ions to the same velocity. For unknown reasons it turned out at the end of the beamtime that the two were not ideally matched. Since the average force of the RF bucket during one revolution is stronger than the cooling force of the electron cooler, we have determined the effective mismatch as a voltage difference between the electron cooler set-point and the real ion beam velocity, which was found to be $67(5)\,$V. This is also included in table 3.

Due to the large uncertainty arising from the electron-cooler calibration, we have examined the possibility to use the previous determination of the hydrogen-like transition wavelength as an alternative way to determine the ion speed. One might argue that the value reported by Klaft and coworkers [14] is less affected by the high-voltage issue since (*i*) the measurement was performed much closer in time to the calibration of the voltmeter at the PTB and (*ii*) a much lower high-voltage of only $120\,$kV was used which does not require such a far extrapolation as in our case. Hence, we have used $\lambda_{0,\text{Klaft}}^{(82+)}$ and $\lambda_{\text{lab}}^{(82+)}$ from (6) to determine the electron cooler voltage

$$eU = (\gamma - 1)\,m_e c^2 = \left[\frac{\lambda_{\text{lab}}^{(82+)}}{2\lambda_0^{(82+)}} \left(\frac{\lambda_0^{(82+)}}{\lambda_{\text{lab}}^{(82+)}} + 1 \right) - 1 \right] m_e c^2 \qquad (10)$$

with a result of $U = 213.770(110)\,$V. This is more than $230\,$V off from our calibration result, a difference corresponding to about 2 times the stated uncertainty.

In the following we determine first the rest-frame transition frequencies for both charge states using our cooler calibration independent of the previous measurement and evaluate the specific difference $\Delta'E$. Then we return to the value of Klaft and coworkers and the consequences of this deviation for $\Delta'E$ and the test of the QED calculation.

The rest frame HFS-transition wavelengths are calculated using the relativistic Doppler formula $\lambda_0 = \lambda_{\text{lab}} \cdot \gamma\,(1 \mp \beta)$ and (8) for Bi^{82+}and Bi^{80+}. The values and

Table 4. Wavelengths and transition energies of the HFS-transitions in highly charged [209]Bi and the specific difference $\Delta'E$ according to equation (1). All values were obtained using ion speed determination from the electron cooler voltage with all corrections and uncertainties as described in the text and listed in table 3. The dominant uncertainty (second parentheses) of our values reported previously in [1] arises from the electron-cooler voltage-calibration uncertainty, while the first one arises in about equal parts from the laboratory wavelength uncertainty given in (6) and (7) and other voltage uncertainty contributions.

	[nm]	[meV]	Ref
Bi[82+]	243.75(2)(5)	5086.3(3)(11)	[1]
	243.87(4)	5084.1(8)	[14]
Bi[80+]	1554.66(10)(33)	797.50(5)(17)	[1]
	1511(50)	820(26)	[20]
$\Delta'E$	-	$-61.37(8)(35)$	
$\Delta'E$ (Theory)	-	$-61.320(6)$	

uncertainties are summarized in table 4. Our value for the HFS in Bi[82+] resulting from this analysis and presented before in [1] is two orders of magnitude more precise than the only experimental value reported previously, determined indirectly via x-ray emission spectroscopy [20].

Our value for the hydrogen-like ion is considerably different from the previous one but the error bars representing the systematic uncertainties do almost overlap. The left part of figure 7(a) shows the wavelength of both transitions obtained with our cooler calibration. Error bars represent the uncertainty contributions without (red) and including (black) the dominant uncertainty arising from the electron-cooler calibration. Also shown (indicated as $\lambda_{\mathrm{H,this}} + \Delta'E$) is the prediction for the wavelength of the Li-like Bi of $\lambda = 1554.56(18)\,\mathrm{nm}$ based on $\Delta'E$ as listed in table 2 and our transition wavelength for H-like Bi. Please note that the correlated uncertainty of the voltage calibration is neglected here, since both our measurements were made using the same calibration. However, the contribution of $25\,\mathrm{V}$ corresponding to the electron cooler reproducibility (which is about 22% of the total systematic uncertainty) and the statistical uncertainty have been taken into account. The expected value and our experimental result are consistent. On the right side of figure 7(a) the wavelength of H-like Bi from Klaft *et al.* [14] is shown for comparison. Moreover, the predicted wavelength for Li-like Bi based on this value and $\Delta'E$ is also indicated. As discussed above, we can use the old H-like wavelength as a reference and calibrate our voltage if we further presume that (an assumed) miscalibration affects both our measurements in the same way. Since the hydrogenlike and the lithiumlike measurements are performed at almost equal velocity, we can calculate this in an easy way using

$$\lambda_{\mathrm{lab}}^{(82+)} \cdot \lambda_{\mathrm{lab}}^{(80+)} = \lambda_0^{(82+)} \gamma \left(1 + \beta\right) \cdot \lambda_0^{(80+)} \gamma \left(1 - \beta\right) \quad = \lambda_0^{(82+)} \cdot \lambda_0^{(80+)} \quad (11)$$

where we have neglected the tiny voltage difference of $70\,\mathrm{V}$ giving rise to a velocity change of $\delta\beta \approx 7 \cdot 10^{-5}$ between the two measurements. Solving equation (11) for the

rest-frame transition wavelength of the lithium-like ion $\lambda_0^{(80+)}$ and using the value from Klaft and coworkers for $\lambda_0^{(82+)}$ as well as our laboratory wavelengths (6) and (7) for both species, we obtain

$$\lambda_0^{(80+)} = \frac{\lambda_{\text{lab}}^{(82+)} \cdot \lambda_{\text{lab}}^{(80+)}}{\lambda_0^{(82+)}} = 1554.16(27)\,\text{nm}, \tag{12}$$

which is more than 0.5 nm smaller than the predicted value. Performing the full calculation, including the electron-cooler voltage difference of 70 V between the measurements of Bi^{82+} and Bi^{80+}, we obtain $\lambda_0^{(80+)} = 1553.96(29)\,\text{nm}$, even further away from the predicted wavelength and depicted as blue square in figure 7(a). Our measured laboratory-frame wavelengths are therefore strongly inconsistent with the assumption that both, $\Delta E^{(1s)}$ from Klaft *et al.* and the specific difference $\Delta'E$ are correct. We will finally analyze the results of both calibrations for $\Delta'E$.
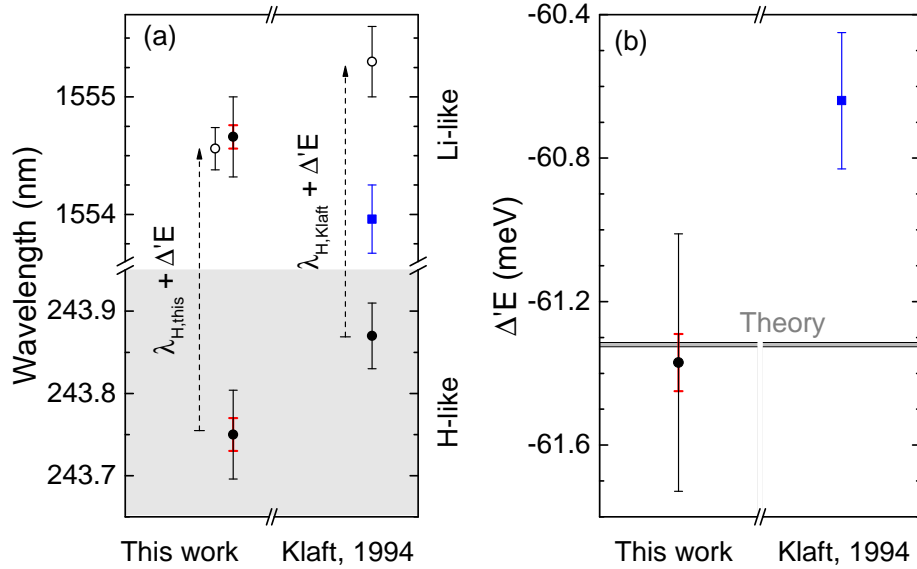
Figure 7. (a) Wavelengths of the transitions in hydrogen-like and lithium-like bismuth. The black filled circles are the experimental results for $\text{Bi}^{80+,82+}$ from [1] and Bi^{82+} reported in [14]. Each is based on the respective electron-cooler calibration at the time. Red and black error bars are neglecting and including the electron-cooler voltage uncertainty, respectively. The open circles are the transition wavelengths corresponding to the hyperfine splitting energy in Bi^{80+} calculated as $\Delta E^{(2s)} = \xi \Delta E^{(1s)} + \Delta'E$ with the respective value of $\Delta E^{(1s)}$ as indicated (details see text). The blue filled square is the wavelength determined for Bi^{80+} from our measurement in [1] with a voltage calibration adapted to reproduce the value for Bi^{82+} from [14] (see equation (11) and following text. (b) Specific difference $\Delta'E$ of the hyperfine splittings in Bi^{82+} and Bi^{80+}. The black filled circle is calculated using the experimental values shown on the left of figure (a), which are based on the latest electron-cooler calibration. Contrary, the blue square is obtained from the two experimental values depicted on the right side of (a). The double line indicates the uncertainty interval of the theoretical result.
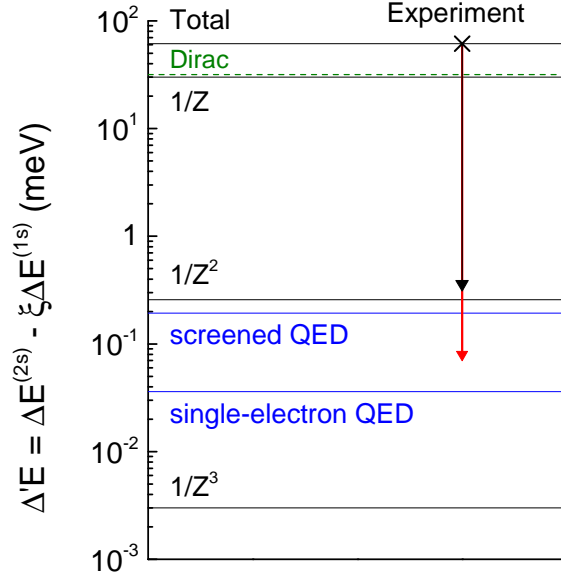
Figure 8. Individual contributions to $\Delta'E$ according to table 2. The uppermost line represents the total value, the dotted line is the contribution from the specific difference of the Dirac values for the hydrogen-like and the lithium-like ion, while the other lines represent the contributions of the electron-electron interaction which is expanded in powers of $1/Z$. The two blue lines indicate the QED contribution from the screened QED and from the single-electron QED. The experimental sensitivities are given by the red and black arrows, representing the uncertainty without and including the electron-cooler voltage uncertainty, respectively. Only the systematic uncertainty caused by the high-voltage measurement prevents a test of the screened QED.

4.3. Specific difference $\Delta'E$

In the last two rows of table 4 the specific difference $\Delta'E$ is given as calculated from our experimental transition wavelengths and compared to the predicted value from theory. They are in excellent agreement, even within the statistical uncertainty, as can also be seen in figure 7(b) (black filled circle). In figure 8 the individual contributions to $\Delta'E$ which are free of experimental input are shown as listed in table 2 and the arrows represent the experimental sensitivity to the contributions according to the statistical and the systematic uncertainty. Our result confirms the total calculated value of the specific difference on a 6×10^{-3} level.

About half of the specific difference arises from the interelectronic-interaction correction in Li-like bismuth. Being up to 70% of relativistic origin, it can only be evaluated within a rigorous QED approach. Thus, we have effectively tested the relativistic interelectronic-interaction in the presence of a strong magnetic field in a heavy highly charged ion for the first time and reached an accuracy at the 1% level. To achieve this accuracy in the calculations, theory has to go beyond the Coulomb approximation and needs to include the Breit interaction. The Breit term accounts for magnetic interactions and retardation effects to the order of $1/c^2$ and represents

about 2.2% of the total value of $\Delta'E$ [47] – its importance has been unambiguously confirmed by our result. A measurement with similar statistical uncertainty but a better control on the voltage systematic will allow for a first test of the screened QED contributions. Such a measurement has been performed in the meantime at the ESR using a 200-kV high-voltage divider and further improvements in data acquisition, but analysis of this data is still ongoing. First results have already been presented in [36] and results of a partial analysis of a subsection of hydrogen-like data is in reasonable agreement with the result of the experiment reported here. QED on the single-electron level does unfortunately largely cancel in $\Delta'E$ and a reasonable test of this contribution requires further reduction of the uncertainty in both transitions by at least one order of magnitude. This improvement cannot be achieved at a storage ring. Therefore the SpecTrap Penning trap is currently being installed at the HITRAP facility [46] at the GSI Helmholtz Centre for Heavy Ion Research that is especially designed for laser spectroscopy on the ground state of hydrogen-like and lithium-like heavy ions [48, 49, 50].

Acknowledgment

References

[1] Lochmann M *et al* 2014 *Phys. Rev. A* **90** 030501.
[2] Hanneke D, Fogwell S and Gabrielse G 2008 *Phys. Rev. Lett.* **100** 120801.
[3] Weitz M, Schmidt-Kaler F and Hänsch T W 1992 *Phys. Rev. Lett.* **68** 1120.
[4] Hagley E W and Pipkin F M 1994 *Phys. Rev. Lett.* **72** 1172.
[5] Kolachevsky N *al* 2009 *Phys. Rev. Lett.* **102** 213002.
[6] Pohl R *et al* 2016 *Science* **353** 669.
[7] Sturm S, Wagner A, Schabinger B, Zatorski J, Harman Z, Quint W, Werth G, Keitel C H and Blaum K 2011 *Phys. Rev. Lett.* **107** 023002.
[8] Köhler F *et al* 2016 *Nat. Commun.* **7** 10246.
[9] Gumberidze A *et al* 2005 *Phys. Rev. Lett.* **94** 233001.

[10] Beiersdorfer P 2010 *J. Phys. B: At. Mol. Opt. Phys.* **43** 074032.
[11] Pohl R 2010 *Nature* **466** 213.
[12] Antognini A *et al* 2013 *Science* **339** 417.
[13] Werth G 2006 *Hyperfine Interac.* **172** 125.
[14] Klaft I *et al* 1994 *Phys. Rev. Lett.* **73** 2425.
[15] Seelig P *et al* 1998 *Phys. Rev. Lett.* **81** 4824.
[16] Crespo López-Urrutia J R, Beiersdorfer P, Savin D W and Widmann K 1996 *Phys. Rev. Lett.* **77** 826.
[17] Crespo López-Urrutia J R, Beiersdorfer P, Widmann K, Birkett B B, Mårtensson-Pendrill A-M and Gustavsson M G H 1998 *Phys. Rev. A* **57** 879.
[18] Beiersdorfer P *et al* 2001 *Phys. Rev. A* **64** 032506.
[19] Shabaev V M, Artemyev A N, Yerokhin V A, Zherebtsov O M and Soff G 2001 *Phys. Rev. Lett.* **86** 3959.
[20] Beiersdorfer, Osterheld P A L , Scofield J H, Crespo López-Urrutia J R and Widmann K 1998 *Phys. Rev. Lett.* **80** 3022.
[21] Ramsey N F 1993 *Hyperfine Interac.* **81** 97.
[22] Beier T 2000 *Phys. Rep.* **339** 79.
[23] Boucard S and Indelicato P 2000 *Eur. Phys. J. D* **8** 59.
[24] Tomaselli M, Kühl T, Nörtershäuser W, Borneis S, Dax A, Marx D, Wang H and Fritzsche S 2002 *Phys. Rev. A* **65** 022502.
[25] Shabaev V M, Shabaeva M B, Tupitsyn I I, Yerokhin V A, Artemyev A N, Kühl T, Tomaselli M and Zherebtsov O M 1998 *Phys. Rev. A* **57** 149.
[26] Volotka A V, Glazov D A, Andreev O V, Shabaev V M, Tupitsyn I I and Plunien G 2012 *Phys. Rev. Lett.* **108** 073001.
[27] Shabaev V M, Shabaeva M B, Tupitsyn I I, Yerokhin V A, Artemyev A N, Kühl T, Tomaselli M and Zherebtsov O M 1998 *Phys. Rev. A* **58** 1610 Errata.
[28] Tomaselli M, Fritzsche S, Kühl T and Winter H 2000 *Hyperfine Interact* **127** 315.
[29] Shabaev V M, Artemyev A N, Zherebtsov O M, Yerokhin V A, Plunien G and Soff G 2000 *Hyperfine Interact.* **127** 279.
[30] Sapirstein J and Cheng K T *Phys. Rev. A* **63** 032506.
[31] Franzke B 1987 *Nucl. Instrum. Meth. B* **24-25** 18.
[32] Brown I G 1994 *Rev. Sci. Instrum* **65** 3061.
[33] Nolden F *et al* 2011 *Nucl. Instrum. Meth. A* **659** 69.
[34] Steck M, Beller P, Beckert K, Franzke B and Nolden F 2004 *Nucl. Instrum. Meth. A* **532** 357.
[35] Winters D *et al* 2015 *Phys. Scr.* **T166** 014048.
[36] Ullmann J *et al* 2015 *J. Phys. B: At. Mol. Opt. Phys.* **48** 144022.
[37] Wen W *et al* 2013 *Nucl. Instrum. Meth A* **711** 90.
[38] Vollbrecht J *et al* 2015 *J. Phys. Conf. Ser.* **583** 012002.
[39] Winter H 1999 PhD Thesis, Technische Universität, Darmstadt.
[40] Hannen V *et al* 2013 *J. Instrum.* **8** 09018.
[41] Weber G *et al* 2009 *Phys. Rev. ST Accel. Beams* **12** 084201.
[42] Andreev O V, Glazov D A, Volotka A V, Shabaev V M and Plunien G 2012 *Phys. Rev. A* **85** 022510.
[43] Lochmann M 2013 PhD Thesis, Johannes Gutenberg-Universität, Mainz.
[44] Jöhren R 2013 PhD Thesis, Westfälischen Wilhelms-Universität, Münster.
[45] Poth H 1990 *Phys. Rep.* **196** 135 .
[46] Kluge H-J *et al* 2008 *Adv. Quantum Chem. 53* **83**.
[47] Volotka A V 2016 (private communication).
[48] Andelkovic Z, Cazan R, Nörtershäuser W, Bharadia S, Segal D M, Thompson R C, Jöhren R, Vollbrecht J, Hannen J and Vogel M 2013 *Phys. Rev A* **87** 033423.
[49] Andelkovic Z *et al* 2015 *Hyperfine Interact.* **235** 37.

[50] Murböck T, Schmidt S, Birkl G, Nörtershäuser W, Thompson R C and Vogel M 2016 *Phys. Rev. A* **94** 043410.